www.sciencemag.org/cgi/content/full/science.aar8658/DC1

Supplementary Materials for

Large-scale ocean deoxygenation during the Paleocene-Eocene Thermal Maximum

Weiqi Yao*, Adina Paytan, Ulrich G. Wortmann

*Corresponding author. Email: weiqi.yao@mail.utoronto.ca

Published 19 July 2018 on *Science* First Release
DOI: 10.1126/science.aar8658

This PDF file includes:

Materials and Methods
Figs. S1 to S8
Tables S1 and S2
References

Materials and Methods

We use a modified sequential leaching method (*11*) to extract marine barite crystals in sediments from Ocean Drilling Program (ODP) Leg 199 Hole 1221C (Core 11X-3), which was located in the equatorial Pacific upwelling zone during the PETM (3.1 ºN, 116.5 ºW, palaeo-depth ~3000 m) (*1, 22*), and ODP Leg 208 Hole 1263C (Core 14H-2 and 14H-CC) and Hole 1265A (Core 29H-6 and 29H-7) in the South Atlantic (*28*). All samples are analyzed with continuous flow isotope ratio mass spectrometer system (CF-IRMS, Finnigan MAT 253 in continuous flow mode using the Conflo III open split interface) at the Department of Earth Sciences (University of Toronto). The $\delta^{34}S$ values are calibrated using three international standards (*29*) with respect to Vienna Canyon Diablo Troilite (VCDT): NBS 127 (21.12 ‰), IAEA-SO-5 (0.49 ‰) and IAEA-SO-6 (-34.05 ‰).

Supplementary Text

Potential Diagenetic Effects

There are two processes which could affect our measured barite sulfur isotope ratios. A) If the organic matter concentration in the sediment increases, so could the concentration of pyrite. If we get a sizable concentration of sedimentary pyrite, it could contaminate the barite S-isotope measurement. This would lead to a negative excursion, which is clearly not the case. Moreover, barite is separated under an N_2 atmosphere to prevent oxidation of S and formation of barite during the chemical treatment and all of our samples are inspected for purity under the SEM and did not show any contaminating pyrite. B) Barite can dissolve and re-precipitate if the sulfate concentration in the porewater drops to zero. The modern day porewater shows no such depletion at these sites, however, it is conceivable that a transient depletion happened during the PETM. Processes like these have been observed with black shale layers. However, diagenetic fronts typically occur on the top or above of these layers (e.g., *30*) which is not the case for these sites.

Further evidence comes from investigating the morphology and the Ca, and Sr isotope ratios of our samples. The morphology of diagenetic and hydrothermal barite is distinctively different from authigenic barite (*31*). The ODP Leg 199 Hole 1221C Core 11X-3 samples have been screened by scanning electron microscope (*32, 33*), and do not show any signs of diagenesis, or the presence of hydrothermal barite.

Likewise, diagenetic and/or hydrothermal barite show $\delta^{87}Sr$ and $\delta^{44}Ca$ ratios which are distinctively different from authigenic barite in seawater (*31, 32, 34, 35*). The Hole 1221C data show $\delta^{44}Ca$ values indicative of pelagic barite and demonstrating the absence of hydrothermal or diagenetic values (*33*). The strontium isotopes values of our samples show an average $\delta^{87}Sr$ value of 0.70776 ± 0.00003 (2σ) (*33*), which is consistent with the value of contemporaneous seawater (0.70770 – 0.70785) (*36*). We present these data in the form of cross-plots in Figs. S1 and S2.

Statistical Analysis

In order to test the significance of the observed isotope excursion, we group our data into two groups (Fig. S4). One contains the measurements “inside” the excursion, and the other one contains the data “outside” the excursion.

A box plot of both groups showing the data distribution, the standard deviation, and the mean shows that both groups have not much overlap (Fig. S3).

Next we use the Fisher F-test, to see whether the variances of the two groups are homogeneous. Since they are not, we use a t-test algorithm which accounts for homogeneous variances (the so called Welch t-test).In a subsequent step we use the Welch t-test to test the null hypothesis that both sample sets are statistically equal. The resulting value is t = 4.84 which is larger than the t-value for 10 degrees of freedom at a confidence interval of 99.995 % (4.587). We can thus conclude that the mean of the two groups are significantly different at a confidence level higher than 99.995 %. The p-value for this calculation is 0.0007, significantly below the 0.05 threshold.

We note that with empirical data obtained for reconstruction of geological records a consistent trend with depth/age of a record (rather than scatter in the data) particularly when seen in data from multiple sites with distinct burial histories is on itself considered to be indicative of representing a real trend of change over time. Moreover, the temporal shift over time (~1 ‰) is much larger than the analytical error (1-σ mean: 0.11-0.22 ‰) or the range of values within each time interval (Fig. S3).

The $\delta^{34}S$ value of seawater sulfate at any given time (t) depends to a certain degree on the $\delta^{34}S$ value of seawater sulfate at a given time before ($t - \Delta t$). This allows us to apply a "local regression smoothing" technique (LOESS) (*37*) to estimate the actual $\delta^{34}S$ value of seawater sulfate. We use the default LOESS module provided by the statistical software package R (*38*). The 95 % confidence interval is calculated for each data point from the standard errors returned by the LOESS function. Note that we did not exclude any data points in the statistical treatments above.

Age Model

To model the S-isotope data during the PETM we use the published timescales for our respective drill sites (*1, 39, 40*). In the absence of data to the contrary, we interpolate sedimentation rates linearly between the known datum points (Fig. S5). For modeling purposes, we express time relative to the onset of the PETM as defined by *Nunes and Norris (2005)* (Fig. S6).

The Sulfur Cycle Model

To reconstruct changes in the sulfur cycle during the PETM, we use a box model to simultaneously monitor changes in sulfate concentration and the $\delta^{34}S$ isotope ratio. We use an ocean volume of 1.38×10^{18} m^3 with a sulfate concentration of 5 mM (*9*). The model calculates the seawater sulfate concentration from the balance of the input and output fluxes as:

$$\frac{d}{dt}M_{SO4}(t) = Fw_{SO4} + Fw_{FeS2} + Fw_{FeS2}\big(A(t)\big) + Fv_{SO4} - Fb_{SO4} - Fb_{FeS2} - Fb_{FeS2}\big(A(t)\big) \qquad (1)$$

where MSO4 denotes mass of seawater sulfate; Fw_{SO4}, Fv_{SO4} and Fb_{SO4} denote the evaporite weathering flux, volcanic degassing flux and evaporite burial flux which are assumed to be constant throughout the model run; $Fw_{FeS2}(A)$ and $Fb_{FeS2}(A)$ denote the pyrite weathering and burial fluxes as a function of shelf area A, which itself depends on sea level L; Fw_{FeS2} and Fw_{SO4} denote the portion of the pyrite weathering/burial which is not affected by sea-level changes (see below).

The masses of ^{32}S and ^{34}S of seawater sulfate are calculated accordingly as:

$$\frac{d}{dt}M_{32SO4}(t) = Fw_{32SO4} + Fw_{Fe32S2} + Fw_{Fe32S2}\big(A(t)\big) + Fv_{32SO4} - Fb_{32SO4} - Fb_{Fe32S2} - Fb_{Fe32S2}\big(A(t)\big) \quad (2)$$

Note that $Fb_{32\,SO4}$ (t) changes with time because the $\delta^{34}S$ isotope ratio of evaporite burial is a function of seawater sulfate $\delta^{34}S$.

A similar equation applies to $\delta^{34}S$. The individual fluxes of ^{32}S and ^{34}S can be calculated from the respective $\delta^{34}S$ values as:

$$32S = \frac{1000 \times S}{(\delta 34S + 1000) \times R + 1000} \quad (3)$$

$$34S = S - 32S \quad (4)$$

where S denotes the mass of sulfur and R denotes the isotopic reference ratio (0.044162589) for VCDT (*41*).

We start our model before the onset of the PETM to establish an initial steady state before exploring the S-cycle perturbations. To achieve steady state, we calculate the pyrite burial flux as:

$$Fb_{FeS2} + Fb_{FeS2}\big(A(t)\big) = Fw_{SO4} + Fw_{FeS2} + Fw_{FeS2}\big(A(t)\big) + Fv_{SO4} - Fb_{SO4} \quad (5)$$

and the ^{32}S output flux as:

$$Fb_{FeS2} + Fb_{FeS2}\big(A(t)\big) = Fw_{SO4} + Fw_{FeS2} + Fw_{FeS2}\big(A(t)\big) + Fv_{SO4} - Fb_{SO4} \quad (6)$$

The ^{34}S flux is then determined by:

$$Fb_{34FeS2} + Fb_{34FeS2}\big(A(t)\big) = Fw_{34SO4} + Fw_{Fe34S2} + Fw_{Fe34S2}\big(A(t)\big) + Fv_{34SO4} - Fb_{34SO4} \quad (7)$$

Using the isotope values in Table S2, our model achieves equilibrium for a pyrite burial flux 6.21795×10^{11} mol/yr with an isotopic value of -25.75 ‰. This corresponds to a seawater pyrite offset of 43.35 ‰ (=17.6+25.75 ‰), which is similar to the values used in other sulfur cycle models (*4, 42-45*).

Pyrite Burial and Pyrite Weathering

It is generally assumed that the majority of pyrite burial occurs on continental shelves where sedimentation rates are high and organic matter supply is plentiful (*46, 47*). As such, pyrite weathering and pyrite burial rates are a function of shelf area, which itself depends on sea level (*10, 11*). Using previously published parametrizations (*11*) we calculate the shelf area A as:

$$A(t) = A_0 \times (0.307 \times \Delta L(t)^3 + 0.624 \times \Delta L(t)^2 + 0.43 \times \Delta L(t) + 0.07221) \quad (8)$$

where $A(t)$ denotes shelf area an any given time step [m^2]; A_0 denotes the modern global ocean area (3.61×10^{14} m^2) (*48*); ΔL denotes the difference between paleo-sealevel and modern sea level [km].

To accommodate the effect of sea-level variations on pyrite burial, we describe the pyrite burial flux as the sum of two fluxes: A) the sea-level dependent pyrite burial on continental shelves, and B) the pelagic pyrite burial which is not affected by sea-level changes. Here we assume that for the initial steady state, both fluxes are roughly equal and calculate the pyrite burial flux as:

$$Fb_{FeS2} = 3.108975 \times 10^{11} \quad (9)$$

$$Fb_{FeS2}\big(A(t)\big) = 3.108975 \times 10^{11} \times A\,(t)/A_1 \quad (10)$$

where $A(t)$ denotes shelf area at any given time step as calculated by Eq. 8; A_1 denotes the initial shelf area corresponding to the pre-PETM sea level (*11*).

Similar to pyrite burial, the pyrite weathering flux has two components: A) a steady flux derived from the weathering of sulfide minerals which are exhumed by mountain building; and B) a variable flux which reflects the weathering of sulfide minerals when previously flooded shelf areas become sub-aerially exposed during sea-level low-stands (*11*).

We assign the former flux a constant value of 6×10^{11} mol/yr with a $\delta^{34}S$ value of -20 ‰. To calculate the sea-level dependent pyrite weathering flux we make several assumptions which simplify its treatment: 1) The PETM sea level variations were symmetrical, i.e., that the post-PETM sea level was the same as the pre-PETM sea level; 2) We furthermore assume that a sea-level drop would oxidize all of the pyrite which accumulated during the preceding sea-level rise (Eq. 11). We can thus calculate the mass of pyrite buried in response to a sea-level rise in our model as:

$$\Delta M_{FeS2}\big(A(i)\big) = \sum_{i=u-1}^{i=u+n}\big(Fb_{FeS2}\big(A(i)\big) - 6 \times 10^{11}\big) \times \Delta t \quad (11)$$

where i is the iteration counter in our model, u is the first iteration where the sea-level has increased, and n is the number of steps until the sea level reaches its highest value; Δt denotes the model time step (1 kyrs).

Model Forcing

We consider three possibilities: 1) Changes to the pyrite burial on continental shelves in response to changes in sea-level; 2) AMO-driven pyrite burial on continental slopes; 3) The transient storage of hydrogen sulfide in the oxygen minimum zone (OMZ).

(1) Sea Level Variations

Published values for the PETM associated sea-level variations suggest a 25-m sea-level rise (*12*). Our model shows that this would result in the additional burial of 4.45×10^{10} mol pyrite per year, 4 % of the required increase to explain the observed $\delta^{34}S$ shift. If we calculate the areal extent (Eq. 8-11) required to explain the ^{32}S flux changes, we would need to expand the global shelf area by 5 to 12 times of the current size (*48*). Depending on the ratio of shelf versus pelagic pyrite burial this is equivalent to about 13-32 times the size of the contiguous United States. Clearly, these numbers depend on a variety of assumptions, chiefly, the organic matter burial rate, however, they do demonstrate the magnitude of required flux changes.

(2) AMO-driven Pyrite Burial on Continental Slopes

Linking pyrite burial flux to methane flux provides a plausible explanation for the rise in the marine $\delta^{34}S$ ratio during the PETM (*14*). Here we assume the extreme case that all pyrite burial is controlled by anaerobic methane oxidation (AMO) on continental shelves and will not be affected by sea level variations. To match the measured S-isotope ratios of seawater sulfate, we need to increase the pyrite burial flux to 1.7×10^{12} mol/yr for 70 kyrs. This is equivalent to a 2.7-fold increase compared to the initial pyrite burial flux. Following that we assume that all methane has vented, and that AMO ceases globally. In consequence

we set the pyrite burial flux to zero. The model shows that even if we make these rather extreme assumptions, it would take at least 0.2 Myrs to return the marine $\delta^{34}S$ ratio back to its pre-excursion value (Fig. S7D&F).

(3) Sulfur Fluxes in/out of a Transient Reservoir

From a modeling perspective this case requires no special treatment. The flux of reduced sulfur out of the sulfate pool is conceptually similar to the pyrite burial flux. The flux of reduced sulfur back into the sulfate pool can simply be considered as the difference between reduced pyrite leaving the system (i.e., pyrite burial) and reduced pyrite entering the system. As such the flux can carry a positive or a negative sign. In our model we assume that the transfer of reduced sulfur into the OMZ lasted 50 kyrs and that the subsequent reoxidation took 40 kyrs.

To convert between sulfur mass as calculated by our model to volumes of sulfidic water, we consider two scenarios: A) The isotopic fractionation (α) between sulfate and sulfide is limited to 43 ‰ (*7*) and B) where we allow for the complete expression of the sulfate reduction related isotope fractionation (70 ‰) (*8, 49, 50*). These assumptions provide for an upper and lower limit of how much of sulfate needs to be converted to sulfide.

Furthermore, we assume that the mean H_2S concentration within the OMZ is 0.5 mM, well below the 1 mM threshold which could lead to chemocline upwelling and the subsequent release of H_2S into the atmosphere (*17*).

Using these assumptions we can explain the data using the statistical significant maximum of 18.35 ‰ (Fig. 1) in scenario A with the transfer 1.3×10^{17} mol of sulfur from the marine sulfate into the marine H_2S pool, equivalent to a sulfidic water volume of 2.6×10^{17} m^3. Scenario B results in the transfer of 8×10^{16} mol of sulfur, which is equivalent to a sulfidic water volume of 1.6×10^{17} m^3. The highest measured $\delta^{34}S$ value (18.95 ‰), can be explained with a sulfidic water volume of no more than 2.7×10^{17} m^3 for α of 70 ‰ (Fig. S8). If we additionally allow for the effects of AMO-related pyrite burial, these numbers become smaller.

It should be noted that the above model fluxes are net-fluxes, and do not consider the re-oxidation of hydrogen sulfide which diffuses out of the OMZ. This is because the recycling of previously reduced sulfur back into to oxic water, has no net effect on the isotopic ratio of seawater sulfate. It is only the net difference between the fluxes in, and out of, the OMZ which determines the isotopic effect. As such, we do not consider the gross fluxes in our mass balance model above. It does however imply the question whether the microbially mediated reduction of sulfate (MSR) provides enough H_2S to counter this loss.

The rate of microbial sulfate reduction (MSR) is a function of sulfate availability and organic matter quality and quantity (*51*). Assuming vertical advection rates of 4 m/yr (*17*), and a sulfate concentration of 5 mM (*9*) this will supply about 14 mmol/m^2/day of sulfate into the oxygen minimum zone (OMZ). In the modern ocean, the carbon flux out of the euphotic zone varies between 0.1 to 10 mol carbon per m^2/day (*52*) and it may have been larger during the PETM (*53*), so it is evident that MSR is limited by sulfate supply, and not by OM availability. The concentration of oxygen in seawater is about 1 mM, and we need two oxygen molecules to re-oxidize sulfide back to sulfate. Since MSR is capable to provide an H_2S flux of up to 14 mmol/m^2/day, we would need up to 28 mmol/m^2/day

oxygen, whereas the advective supply of oxygen is limited to ~3 mmol/m^2/day. It thus follows that the supply of sulfide outweighs the supply of oxygen. Kump et al. (2005) provide a more robust treatment of this including estimates at what point the gas exchange at the air sea interface is overwhelmed, and free H_2S enters the atmosphere.

Fig. S1.

Cross-plot of the $\delta^{34}S$ and $\delta^{87}Sr$ in barite samples from ODP Hole 1221C Core 11X-3. $\delta^{34}S$ data from this study, and $\delta^{87}Sr$ data after *Griffith et al. (2015)*.

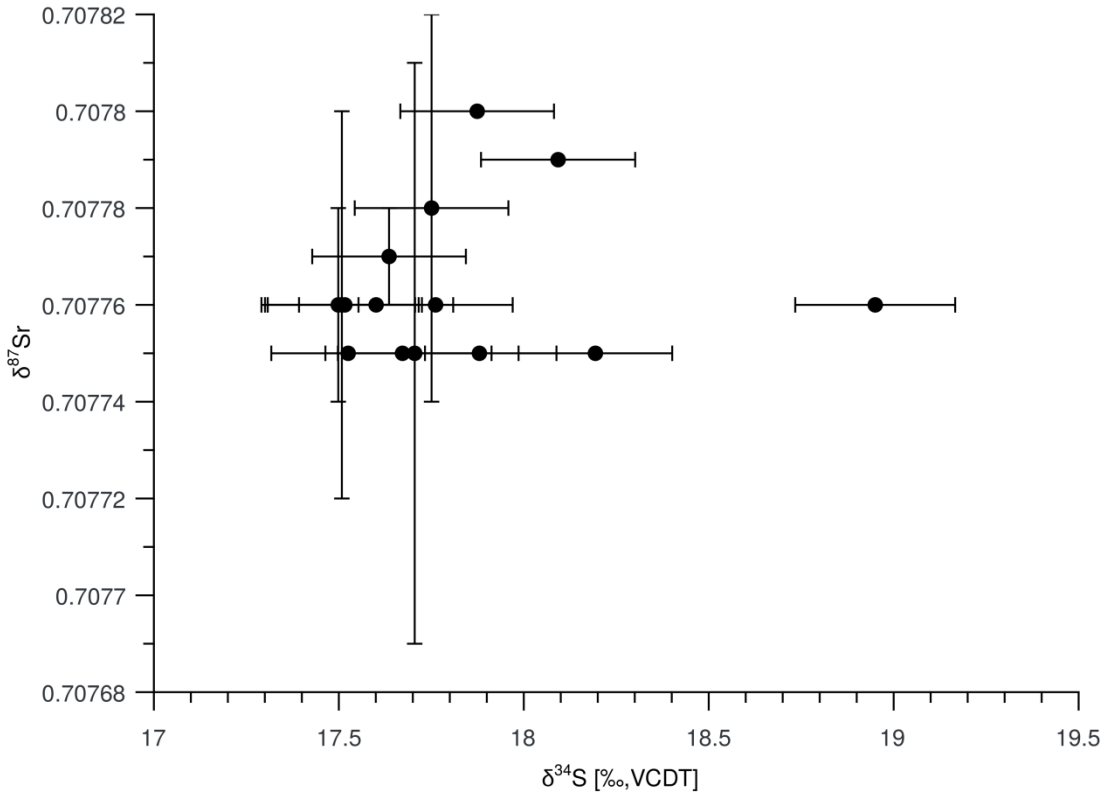

Fig. S2.

Cross-plot of the $\delta^{34}S$ and $\delta^{44}Ca$ in barite samples from ODP Hole 1221C Core 11X-3. $\delta^{34}S$ data from this study; $\delta^{44}Ca$ data after *Griffith et al. (2015)*.

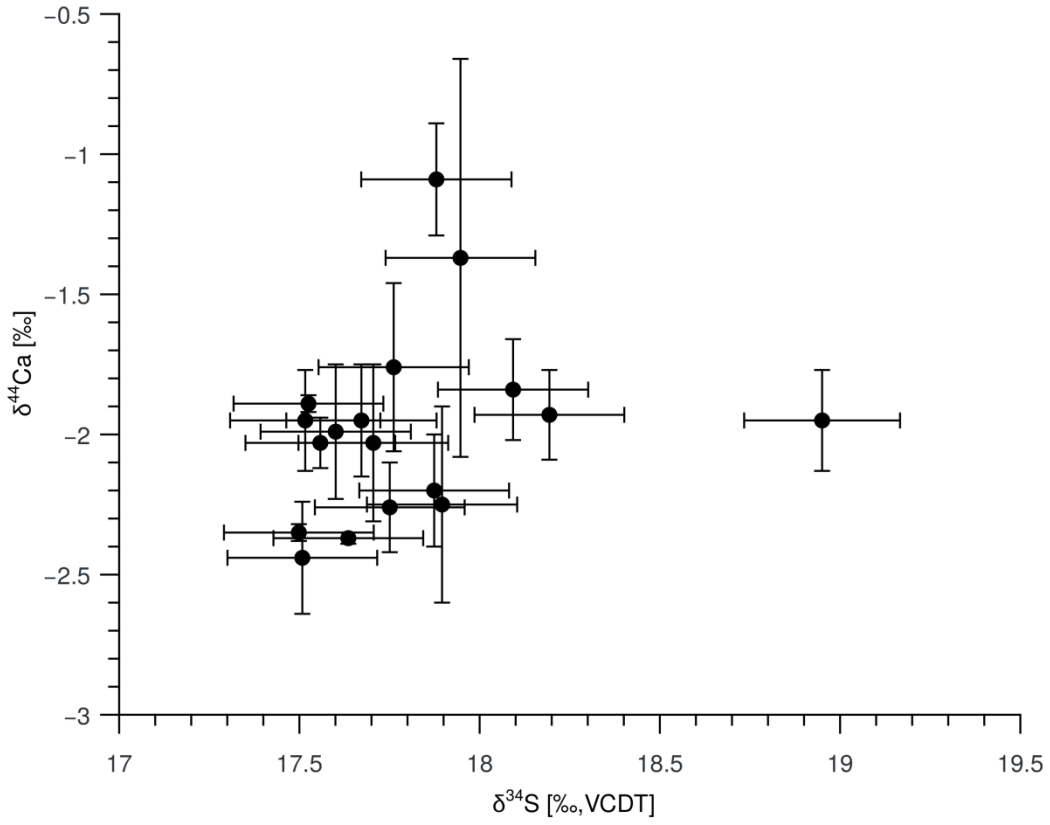

Fig. S3.

Box plot showing the data distribution, the standard deviation, and the mean for samples inside and outside of the PETM peak. See Fig. S4 for the how the samples where categorized.

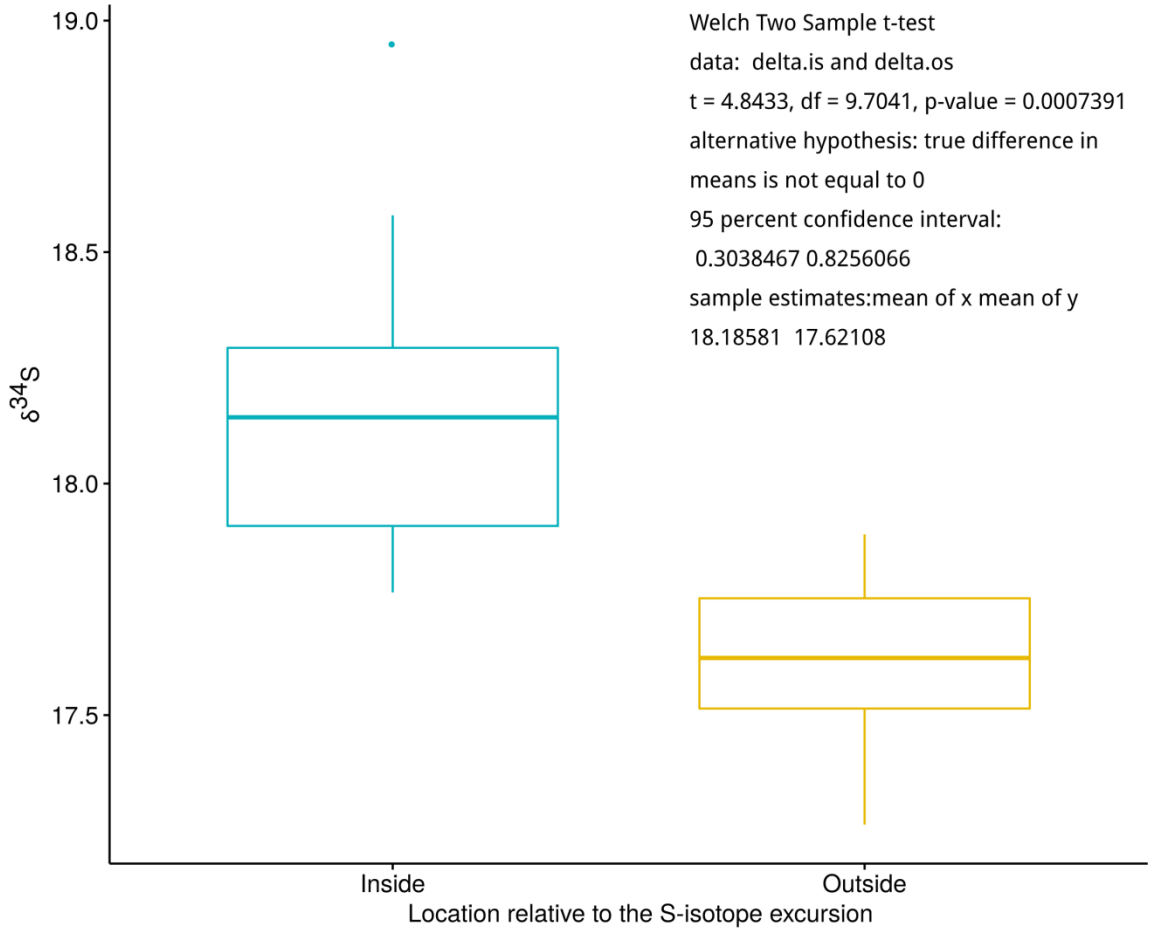

Fig. S4.

The $\delta^{34}S$ measured on authigenic marine barite crystals across the PETM. Black circles and red squares denote the samples groups inside and outside of the PETM $\delta^{34}S$ excursion respectively.

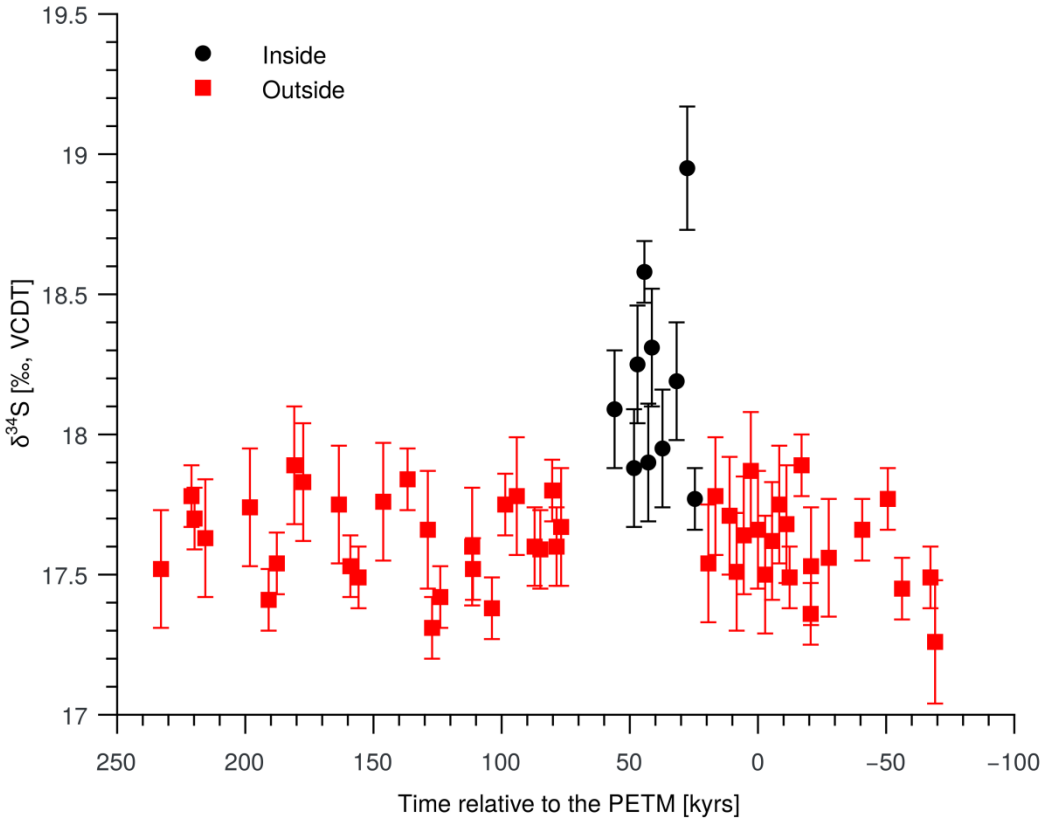

Fig. S5.

Age-depth plot for ODP Hole 1221C Core 11X-3. Ages and PETM stages (shaded areas) as defined by *Nunes and Norris (2005)*.

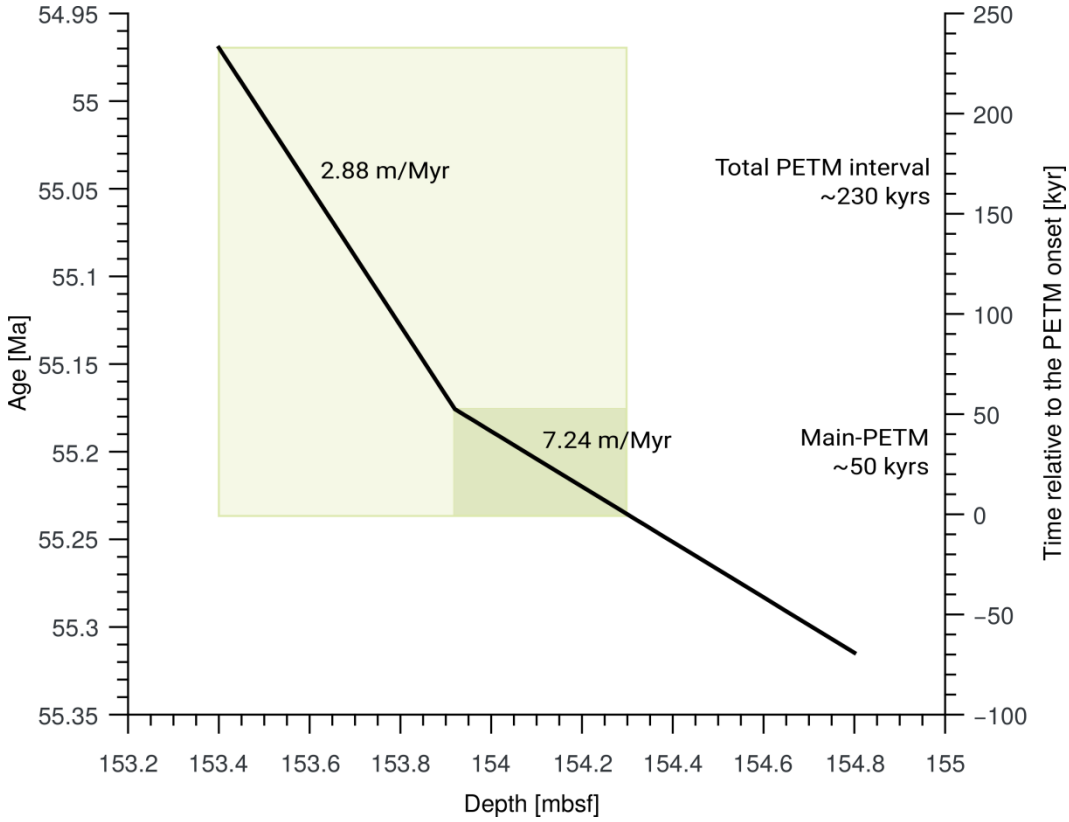

Fig. S6.

The sulfur and carbon isotopes against time from ODP Hole 1221C Core 11X-3. The red curve denotes the 3-point moving average marine $\delta^{34}S$ values (red solid circles) derived from authigenic marine barite in this study; Light grey and dark grey curves denote the 3-point moving average of the $\delta^{13}C$ values of benthic foraminifera (solid diamonds) and bulk carbonate (open diamonds), respectively (*1*). Shaded areas indicate the extents of the PETM interval (*1*).

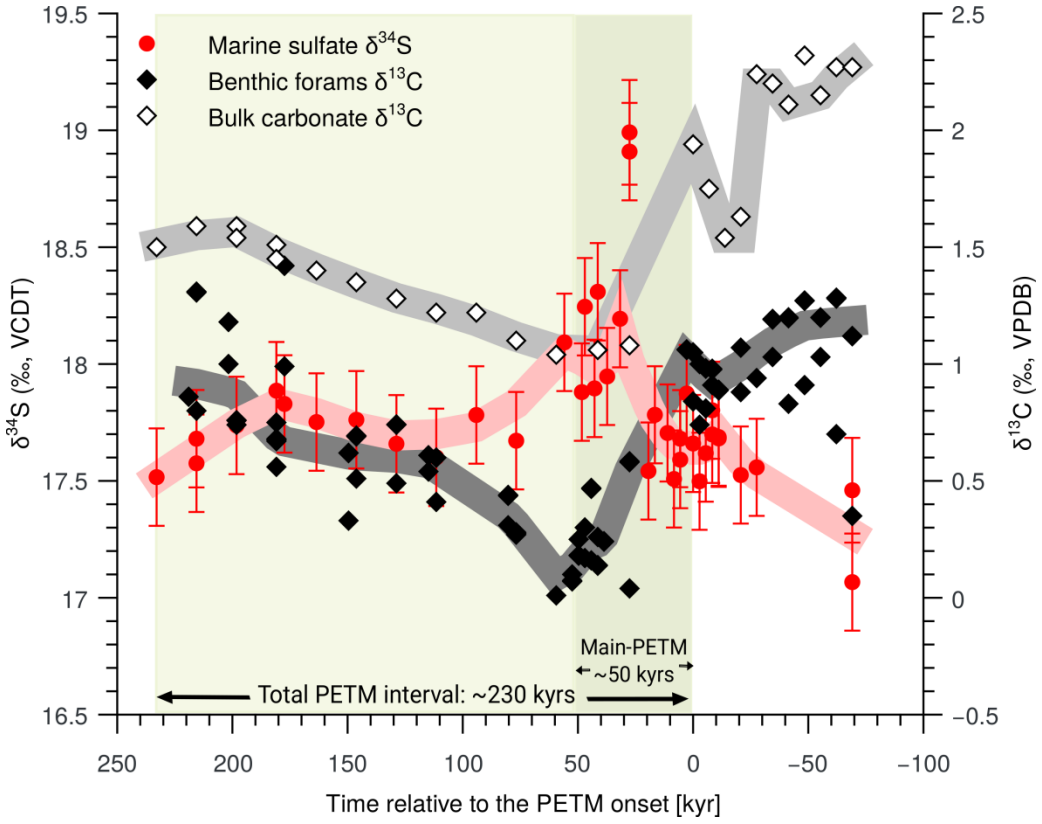

Fig. S7.

AMO-driven pyrite burial on continental slopes and resulting changes in the marine sulfur cycle across the PETM. Given the extreme case that all pyrite burial was AMO-controlled and that no pyrite was buried once the methane stops venting during the PETM, it would take 200 kyrs for the marine sulfur isotope to recover to the pre-excursion value.

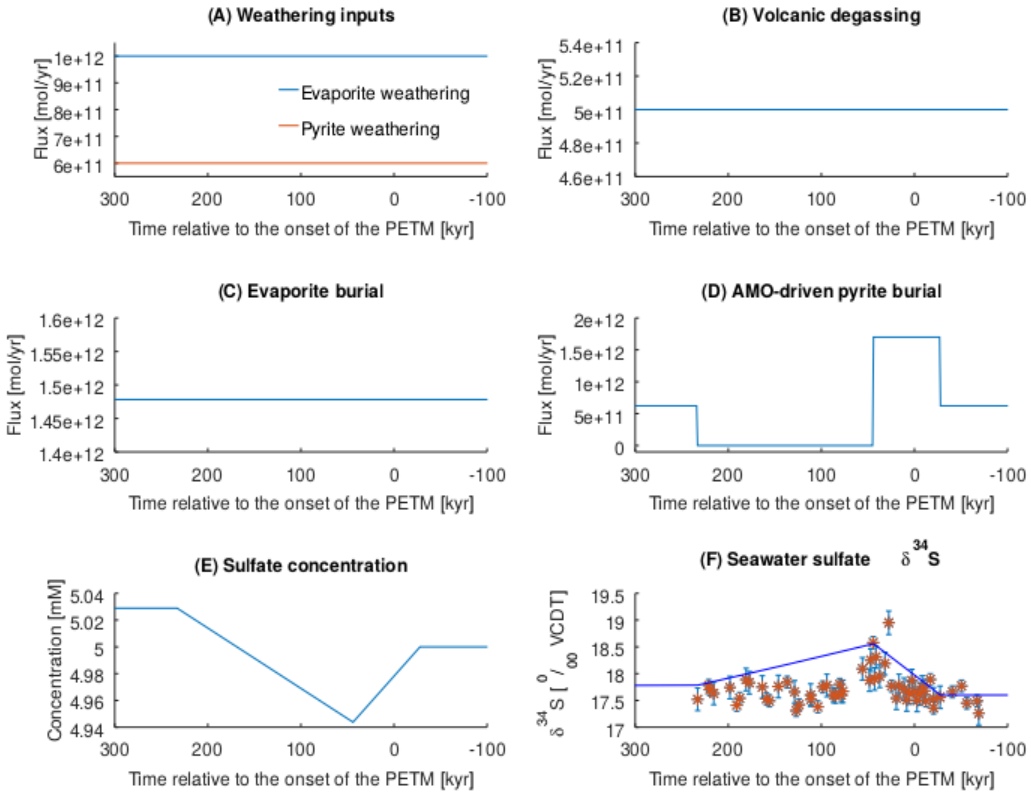

Fig. S8.

Input/output fluxes and resulting changes in the marine sulfate reservoir across the PETM. Note that the pyrite weathering flux increases temporarily with falling sea level (Fig. S8A), and that pyrite burial on continental shelves remains elevated until sea level returns to the pre-PETM value (Fig. S8D). Fig. S8C shows the transfer of ^{32}S in and out of the OMZ. Fig. S8F shows the modelled $\delta^{34}S$ values versus the observed data (asterisk symbols). Green solid lines: model results for scenario A; Deep blue solid lines: model results for scenario B; Black dashed lines: model results assuming the $\delta^{34}S$ value of 18.95 ‰ representative of the maximum S-isotope excursion for α of 70 ‰.

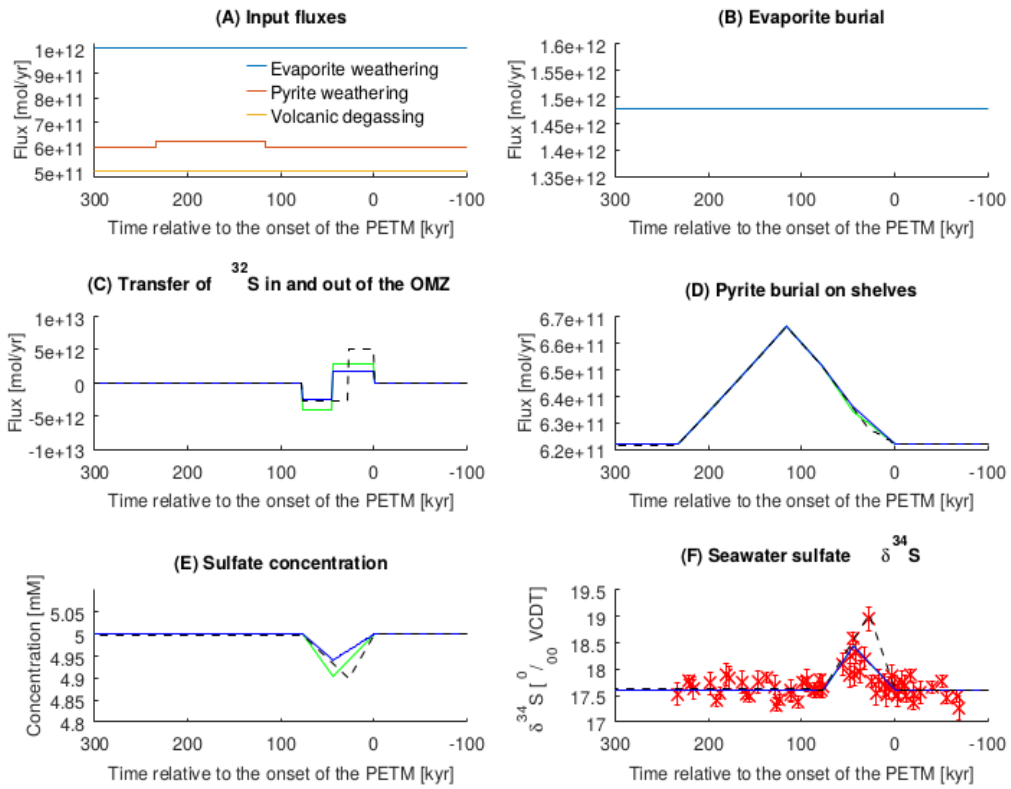

Table S1.

Sample list of the sulfur-isotope data of seawater sulfate

Core, section, interval [cm]	Depth [mbsf]	Time relative to the PETM onset [kyrs]	$\delta^{34}S$ [‰ VCDT]	$\delta^{34}S$ error [‰] (1-σ mean)
1221C 11X-3 140-142	154.80	-69.10	17.26	0.21
1265A 29H-7 148-150	275.87	-67.29	17.49	0.11
1265A 29H-7 128-130	275.67	-56.20	17.45	0.11
1265A 29H-7 118-120	275.57	-50.65	17.77	0.11
1265A 29H-7 100-102	275.39	-40.66	17.66	0.11
1221C 11X-3 110-113	154.50	-27.60	17.56	0.21
1221C 11X-3 105-108	154.45	-20.70	17.53	0.21
1263C 14H-CC 15.5-18	285.57	-20.56	17.36	0.11
1265A 29H-7 80-82	275.19	-17.00	17.89	0.11
1263C 14H-CC 8-10.5	285.49	-12.34	17.49	0.11
1221C 11X-3 98-100	154.38	-11.10	17.68	0.21
1221C 11X-3 96-98	154.36	-8.30	17.75	0.21
1221C 11X-3 94-96	154.34	-5.50	17.62	0.21
1221C 11X-3 92-94	154.32	-2.80	17.50	0.21
1221C 11X-3 90-92	154.30	0.00	17.66	0.21
1221C 11X-3 88-90	154.28	2.80	17.87	0.21
1221C 11X-3 86-88	154.26	5.56	17.64	0.21
1221C 11X-3 84-86	154.24	8.32	17.51	0.21
1221C 11X-3 82-84	154.22	11.08	17.71	0.21
1221C 11X-3 78-80	154.18	16.60	17.78	0.21
1221C 11X-3 76-78	154.16	19.36	17.54	0.21
1263C 14H-2 122-124 *	285.13	24.62	17.77	0.21
1221C 11X-3 70-72 *	154.10	27.60	18.95	0.11
1221C 11X-3 66-70 *	154.07	31.74	18.19	0.22
1221C 11X-3 62-66 *	154.03	37.26	17.95	0.21
1221C 11X-3 60-62 *	154.00	41.40	18.31	0.21
1221C 11X-3 58-62 *	153.99	42.80	17.90	0.21
1265A 29H-7 60-62 *	274.99	44.31	18.58	0.21

1221C 11X-3 56-58 *	153.96	47.00	18.25	0.11
1221C 11X-3 54-58 *	153.95	48.35	17.88	0.21
1221C 11X-3 50-54 *	153.91	55.95	18.09	0.21
1221C 11X-3 45-48	153.85	76.80	17.67	0.21
1265A 29H-7 50-52	274.89	78.57	17.60	0.21
1265A 29H-7 48-50	274.87	80.29	17.80	0.14
1263C 14H-2 62-64	284.53	84.91	17.59	0.11
1265A 29H-7 40-42	274.79	87.14	17.60	0.14
1221C 11X-3 40-43	153.80	94.10	17.78	0.21
1265A 29H-7 30-32	274.69	98.59	17.75	0.11
1263C 14H-2 38-40	284.29	103.79	17.38	0.11
1265A 29H-7 20-22	274.59	111.19	17.52	0.11
1221C 11X-3 35-38	153.75	111.50	17.60	0.21
1265A 29H-7 12-14	274.51	123.94	17.42	0.11
1265A 29H-7 10-12	274.49	127.13	17.31	0.11
1221C 11X-3 30-33	153.70	128.80	17.66	0.21
1265A 29H-7 4-6	274.43	136.70	17.84	0.11
1221C 11X-3 25-28	153.65	146.20	17.76	0.21
1265A 29H-6 142-144	276.31	155.83	17.49	0.11
1265A 29H-6 140-142	274.29	159.01	17.53	0.11
1221C 11X-3 20-23	153.60	163.50	17.75	0.21
1221C 11X-3 16-19	153.56	177.40	17.83	0.21
1221C 11X-3 15-18	153.55	180.90	17.89	0.21
1265A 29H-6 122-124	294.11	187.71	17.54	0.11
1265A 29H-6 120-122	294.09	190.90	17.41	0.11
1221C 11X-3 10-13	153.50	198.20	17.74	0.21
1221C 11X-3 5-8	153.45	215.60	17.63	0.21
1265A 29H-6 100-102	273.89	219.80	17.70	0.11
1265A 29H-6 98-100	273.87	221.00	17.78	0.11
1221C 11X-3 0-3	153.40	232.90	17.52	0.21

Note: The $\delta^{34}S$ data of seawater sulfate are attained from ODP Leg 199 Hole 1221C from the Equatorial Pacific, ODP Leg 208 Hole 1263C and Hole 1265A from the South Atlantic.

* denotes the samples inside of the PETM $\delta^{34}S$ peak. 1-σ mean = mean standard deviation is determined by repeated measurements of standards with a known isotope ratio.

Table S2.
Modelled sulfur fluxes and isotope ratios for the initial steady state.

Parameter	Initial value	Initial $\delta^{34}S$ value [‰]	Sources
Ocean volume [l]	1.38×10^{21}		Reference (*54*)
Sulfate concentration [mM]	5	17.6	References (*55, 56*)
Evaporite weathering [mol/yr]	1×10^{12}	22	References (*6, 42, 43*)
Total pyrite weathering [mol/yr]	6×10^{11} [b]	-20	See Eq. 11, References (*42, 43*)
Volcanic degassing [mol/yr]	5×10^{11}	0	References (*4, 57*)
Evaporite burial [mol/yr]	1.478205×10^{12} [a]	17.6 [a]	References (4, *43-45, 58*)
Pelagic pyrite burial [mol/yr]	3.108975×10^{11} [a]	-25.75 [a]	See Eq. 9-10
Shelf pyrite burial [mol/yr]	3.108975×10^{11} [a, b]	-25.75 [a]	See Eq. 9-10

Note: [a] The initial steady state values calculated from other known parameters. [b] The fluxes affected by shelf area corresponding to sea-level variations.

References and Notes

1. F. Nunes, R. Norris, in *Proceedings of the Ocean Drilling Program, Scientific Results*, P. Wilson, M. Lyle, J. Firth, Eds. (College Station, TX, 2005), vol. 199, pp. 1–12.

2. R. Zeebe, A. Ridgwell, J. Zachos, Anthropogenic carbon release rate unprecedented during the past 66 million years. *Nat. Geosci.* **9**, 325–329 (2016). doi:10.1038/ngeo2681

3. "IPCC, *Climate Change 2013: The Physical Science Basis. Contribution of Working Group I to the Fifth Assessment Report of the Intergovernmental Panel on Climate Change*, T. F. Stocker *et al*., Eds. (Cambridge Univ. Press, 2013).

4. J. C. Walker, Global geochemical cycles of carbon, sulfur and oxygen. *Mar. Geol.* **70**, 159–174 (1986). doi:10.1016/0025-3227(86)90093-9 Medline

5. U. G. Wortmann, B. M. Chernyavsky, Effect of evaporite deposition on Early Cretaceous carbon and sulphur cycling. *Nature* **446**, 654–656 (2007). doi:10.1038/nature05693 Medline

6. G. Claypool, W. Holser, I. Kaplan, H. Sakai, I. Zak, The age curves of sulfur and oxygen isotopes in marine sulfate and their mutual interpretation. *Chem. Geol.* **28**, 199–260 (1980). doi:10.1016/0009-2541(80)90047-9

7. I. Kaplan, K. Emery, S. Rittenberg, The distribution and isotopic abundance of sulphur in recent marine sediments off southern California. *Geochim. Cosmochim. Acta* **27**, 297–331 (1963). doi:10.1016/0016-7037(63)90074-7

8. U. Wortmann, S. Bernasconi, M. Böttcher, Hypersulfidic deep biosphere indicates extreme sulfur isotope fractionation during single-step microbial sulfate reduction. *Geology* **29**, 647–650 (2001). doi:10.1130/0091-7613(2001)029<0647:HDBIES>2.0.CO;2

9. U. G. Wortmann, A. Paytan, Rapid variability of seawater chemistry over the past 130 million years. *Science* **337**, 334–336 (2012). doi:10.1126/science.1220656 Medline

10. A. Turchyn, D. Schrag, Cenozoic evolution of the sulfur cycle: Insight from oxygen isotopes in marine sulfate. *Earth Planet. Sci. Lett.* **241**, 763–779 (2006). doi:10.1016/j.epsl.2005.11.007

11. S. Markovic, A. Paytan, U. Wortmann, Pleistocene sediment offloading and the global sulfur cycle. *Biogeosciences* **12**, 3043–3060 (2015). doi:10.5194/bg-12-3043-2015

12. K. G. Miller, M. A. Kominz, J. V. Browning, J. D. Wright, G. S. Mountain, M. E. Katz, P. J. Sugarman, B. S. Cramer, N. Christie-Blick, S. F. Pekar, The Phanerozoic record of global sea-level change. *Science* **310**, 1293–1298 (2005). doi:10.1126/science.1116412 Medline

13. J. Higgins, D. Schrag, Beyond methane: Towards a theory for the Paleocene–Eocene Thermal Maximum. *Earth Planet. Sci. Lett.* **245**, 523–537 (2006). doi:10.1016/j.epsl.2006.03.009

14. G. Dickens, Down the Rabbit Hole: Toward appropriate discussion of methane release from gas hydrate systems during the Paleocene-Eocene thermal maximum and other past hyperthermal events. *Clim. Past* **7**, 831–846 (2011). doi:10.5194/cp-7-831-2011

15. G. Dickens, J. O'Neil, D. Rea, R. Owen, Dissociation of oceanic methane hydrate as a cause of the carbon isotope excursion at the end of the Paleocene. *Paleoceanography* **10**, 965–971 (1995). doi:10.1029/95PA02087

16. V. Brüchert, B. B. Jørgensen, K. Neumann, D. Riechmann, M. Schlösser, H. Schulz, Regulation of bacterial sulfate reduction and hydrogen sulfide fluxes in the central namibian coastal upwelling zone. *Geochim. Cosmochim. Acta* **67**, 4505–4518 (2003). doi:10.1016/S0016-7037(03)00275-8

17. L. Kump, A. Pavlov, M. Arthur, Massive release of hydrogen sulfide to the surface ocean and atmosphere during intervals of oceanic anoxia. *Geology* **33**, 397–400 (2005). doi:10.1130/G21295.1

18. W. Landing, S. Westerlund, The solution chemistry of iron(II) in Framvaren Fjord. *Mar. Chem.* **23**, 329–343 (1988). doi:10.1016/0304-4203(88)90102-8

19. A. Paulmier, D. Ruiz-Pino, Oxygen minimum zones (OMZs) in the modern ocean. *Prog. Oceanogr.* **80**, 113–128 (2009). doi:10.1016/j.pocean.2008.08.001

20. M. Nicolo, G. Dickens, C. Hollis, South Pacific intermediate water oxygen depletion at the onset of the Paleocene-Eocene thermal maximum as depicted in New Zealand margin sections. *Paleoceanography* **25**, PA4210 (2010). doi:10.1029/2009PA001904

21. A. Dickson, A. Cohen, A. Coe, Seawater oxygenation during the Paleocene-Eocene Thermal Maximum. *Geology* **40**, 639–642 (2012). doi:10.1130/G32977.1

22. A. Winguth, E. Thomas, C. Winguth, Global decline in ocean ventilation, oxygenation, and productivity during the Paleocene-Eocene Thermal Maximum: Implications for the benthic extinction. *Geology* **40**, 263–266 (2012). doi:10.1130/G32529.1

23. X. Zhou, E. Thomas, A. M. E. Winguth, A. Ridgwell, H. Scher, B. A. A. Hoogakker, R. E. M. Rickaby, Z. Lu, Expanded oxygen minimum zones during the late Paleocene-early Eocene: Hints from multiproxy comparison and ocean modeling. *Paleoceanography* **31**, 1532–1546 (2016). doi:10.1002/2016PA003020

24. M. C. Long, C. Deutsch, T. Ito, Finding forced trends in oceanic oxygen. *Global Biogeochem. Cycles* **30**, 381–397 (2016). doi:10.1002/2015GB005310

25. A. Oschlies, K. Schulz, U. Riebesell, A. Schmittner, Simulated 21st century's increase in oceanic suboxia by CO_2-enhanced biotic carbon export. *Global Biogeochem. Cycles* **22**, GB4008 (2008). doi:10.1029/2007GB003147

26. L. Smith, D. Oseid, I. Adelman, S. Broderius, Effect of hydrogen sulfide on fish and invertebrates. Part I – Acute and chronic toxicity studies. *Ecol. Res. Tech. Rep. Ser. No.3* (U.S. Environmental Protection Agency, 1976).

27. L. Stramma, E. D. Prince, S. Schmidtko, J. Luo, J. P. Hoolihan, M. Visbeck, D. W. R. Wallace, P. Brandt, A. Körtzinger, Expansion of oxygen minimum zones may reduce available habitat for tropical pelagic fishes. *Nat. Clim. Chang.* **2**, 33–37 (2012). doi:10.1038/nclimate1304

28. J. Zachos *et al*., *Proceedings of the Ocean Drilling Program, Initial Reports* (College Station, Texas, 2004), vol. 208, pp. 1–112.

29. T. Coplen *et al.*, *Compilation of minimum and maximum isotope ratios of selected elements in naturally occurring terrestrial materials and reagents*. U.S. *Geological Survey Water-Resources Investigations Report*, 01–4222 (2001).

30. S. Henkel, J. M. Mogollón, K. Nöthen, C. Franke, K. Bogus, E. Robin, A. Bahr, M. Blumenberg, T. Pape, R. Seifert, C. März, G. J. de Lange, S. Kasten, Diagenetic barium cycling in Black Sea sediments – A case study for anoxic marine environments. *Geochim. Cosmochim. Acta* **88**, 88–105 (2012). doi:10.1016/j.gca.2012.04.021

31. A. Paytan, S. Mearon, K. Cobb, M. Kastner, *Geol. Soc. Am.* **30**, 747–750 (2002).

32. E. Griffith, E. Schauble, T. Bullen, A. Paytan, Characterization of calcium isotopes in natural and synthetic barite. *Geochim. Cosmochim. Acta* **72**, 5641–5658 (2008). doi:10.1016/j.gca.2008.08.010

33. E. Griffith, M. Fantle, A. Eisenhauer, A. Paytan, T. Bullen, Effects of ocean acidification on the marine calcium isotope record at the Paleocene–Eocene Thermal Maximum. *Earth Planet. Sci. Lett.* **419**, 81–92 (2015). doi:10.1016/j.epsl.2015.03.010

34. A. Paytan, M. Kastner, E. Martin, J. Macdougall, T. Herbert, Marine barite as a monitor of seawater strontium isotope composition. *Nature* **366**, 445–449 (1993). doi:10.1038/366445a0

35. A. Paytan, K. Averyt, K. Faul, E. Gray, E. Thomas, *Geol. Soc. Am.* **35**, 1139–1142 (2007).

36. D. Hodell, G. D. Kamenov, E. C. Hathorne, J. C. Zachos, U. Röhl, T. Westerhold, Variations in the strontium isotope composition of seawater during the Paleocene and early Eocene from ODP Leg 208 (Walvis Ridge). *Geochem. Geophys. Geosyst.* **8**, Q09001 (2007). doi:10.1029/2007GC001607

37. W. Cleveland, Robust Locally Weighted Regression and Smoothing Scatterplots. *J. Am. Stat. Assoc.* **74**, 829–836 (1979). doi:10.1080/01621459.1979.10481038

38. R Core Team, R: *a language and environment for statistical computing*, R Foundation. for Statistical Computing (Vienna, Austria, 2012).

39. J. C. Zachos, U. Röhl, S. A. Schellenberg, A. Sluijs, D. A. Hodell, D. C. Kelly, E. Thomas, M. Nicolo, I. Raffi, L. J. Lourens, H. McCarren, D. Kroon, Rapid acidification of the ocean during the Paleocene-Eocene thermal maximum. *Science* **308**, 1611–1615 (2005). doi:10.1126/science.1109004 Medline

40. U. Röhl, T. Bralower, R. Norris, G. Wefer, New chronology for the late Paleocene thermal maximum and its environmental implications. *Geology* **28**, 927–930 (2000). doi:10.1130/0091-7613(2000)28<927:NCFTLP>2.0.CO;2

41. T. Ding, S. Valkiers, H. Kipphardt, P. De Bièvre, P. D. P. Taylor, R. Gonfiantini, R. Krouse, Calibrated sulfur isotope abundance ratios of three IAEA sulfur isotope reference materials and V-CDT with a reassessment of the atomic weight of sulfur. *Geochim. Cosmochim. Acta* **65**, 2433–2437 (2001). doi:10.1016/S0016-7037(01)00611-1

42. R. Garrel, A. Lerman, Coupling of the sedimentary sulfur and carbon cycles; an improved model. *Am. J. Sci.* **284**, 989–1007 (1984). doi:10.2475/ajs.284.9.989

43. L. Kump, R. Garrels, Modeling atmospheric O_2 in the global sedimentary redox cycle. *Am. J. Sci.* **286**, 337–360 (1986). doi:10.2475/ajs.286.5.337

44. A. Kurtz, L. Kump, M. Arthur, J. Zachos, A. Paytan, Early Cenozoic decoupling of the global carbon and sulfur cycles. *Paleoceanography* **18**, 1090–1103 (2003). doi:10.1029/2003PA000908

45. S. Bottrell, R. Newton, Reconstruction of changes in global sulfur cycling from marine sulfate isotopes. *Earth Sci. Rev.* **75**, 59–83 (2006). doi:10.1016/j.earscirev.2005.10.004

46. R. Berner, Burial of organic carbon and pyrite sulfur in the modern ocean; its geochemical and environmental significance. *Am. J. Sci.* **282**, 451–473 (1982). doi:10.2475/ajs.282.4.451

47. B. Jørgensen, Mineralization of organic matter in the sea bed—The role of sulphate reduction. *Nature* **296**, 643–645 (1982). doi:10.1038/296643a0

48. M. Jacobsen, R. Charlson, H. Rodhe, G. Orians, *Earth System Science: From Biogeochemical Cycles to Global Change* (Elsevier, Amsterdam, 2000).

49. D. Canfield, Biogeochemistry of sulfur isotopes. *Rev. Mineral. Geochem.* **43**, 607–636 (2001). doi:10.2138/gsrmg.43.1.607

50. M. Rudnicki, H. Elderfield, B. Spiro, Fractionation of sulfur isotopes during bacterial sulfate reduction in deep ocean sediments at elevated temperatures. *Geochim. Cosmochim. Acta* **65**, 777–789 (2001). doi:10.1016/S0016-7037(00)00579-2

51. B. Chernyavsky, U. Wortmann, REMAP: A reaction transport model for isotope ratio calculations in porous media. *Geochem. Geophys. Geosyst.* **8**, Q02009 (2007). doi:10.1029/2006GC001442

52. L. Legendre, Flux of particulate organic material from the euphotic zone of oceans: Estimation from phytoplankton biomass. *J. Geophys. Res.* **103**, 2897–2903 (1998). doi:10.1029/97JC02706

53. Z. Ma, E. Gray, E. Thomas, B. Murphy, J. Zachos, A. Paytan, Carbon sequestration during the Palaeocene–Eocene Thermal Maximum by an efficient biological pump. *Nat. Geosci.* **7**, 382–388 (2014). doi:10.1038/ngeo2139

54. K. Burke, A. Sengör, Ten metre global sea-level change associated with South Atlantic Aptian salt deposition. *Mar. Geol.* **83**, 309–312 (1988). doi:10.1016/0025-3227(88)90064-3

55. A. Paytan, M. Kastner, D. Campbell, M. H. Thiemens, Sulfur isotopic composition of cenozoic seawater sulfate. *Science* **282**, 1459–1462 (1998). doi:10.1126/science.282.5393.1459 Medline

56. J. Horita, H. Zimmermann, H. Holland, Chemical evolution of seawater during the Phanerozoic. *Geochim. Cosmochim. Acta* **66**, 3733–3756 (2002). doi:10.1016/S0016-7037(01)00884-5

57. K. Hansen, K. Wallman, Cretaceous and Cenozoic evolution of seawater composition, atmospheric O2 and CO2: A model perspective. *Am. J. Sci.* **303**, 94–148 (2003). doi:10.2475/ajs.303.2.94

58. S. Petsch, R. Berner, Coupling the geochemical cycles of C, P, Fe, and S; the effect on atmospheric O 2 and the isotopic records of carbon and sulfur. *Am. J. Sci.* **298**, 246–262 (1998). doi:10.2475/ajs.298.3.246